Journal of Nanomaterials and Applications

Bending and End-Local von Mises Stresses in Thin-Walled Cantilever Tubes: Effects of Cross-Section, Load, and Length

Ştefan Ţălu [1], Niranjan Patra [2,*], Claudio Larosa [3], Nesrine Haddad [4], Tu Nguyen Sinh [5], Dung Nguyen Trong [5]

[1] The Directorate of Research, Development and Innovation Management (DMCDI), Technical University of Cluj-Napoca, 15 Constantin Daicoviciu St., Cluj-Napoca, 400020, Cluj county, Romania. **E**-mail: stefan.talu@auto.utcluj.ro

[2] Department of Chemistry, Koneru Lakshmaiah Education Foundation, Greenfield, Vaddeswaram, Andhra Pradesh 522502, India.

[3] ENEA – Energy Technologies and Renewable Sources Department (TERIN), ENEA Research Center, Via Anguillarese 301, 00123 Santa Maria di Galeria, Rome, Italy

[4] Laboratory of Physics of Materials and Nanomaterials Applied at Environment (LaPhyMNE), Faculty of Sciences in Gabes, Gabes University, 6072 Gabes, Tunisia.

[5] Department of Technological Physics, Faculty of Applied Sciences, University of Transport Technology, 54 Trieu Khuc, Thanh Xuan, 100000, Hanoi, Vietnam

Article info

Type of articles:

Original research paper

Corresponding author*:

Niranjan Patra:

npatra@kluniversity.in

Abstract: The three-dimensional von Mises equivalent stress (σ_{vM}) in thin-walled cantilever tubes is investigated using finite element analysis (COMSOL Multiphysics 6.0) and decomposed against Euler–Bernoulli beam theory to separate global bending from localized boundary effects. Three parameter groups are varied independently: cross-sectional geometry (circular, triangular, square, and rectangular), transverse tip edge load (F = 100–200 N), and tube length (L = 300–400 mm, corresponding to slenderness ratios L/D_o = 5.0–6.7 for the circular tube). Modeled as homogeneous, isotropic, linearly elastic AISI 4340 steel, the stress field is governed by Beltrami–Michell compatibility and is therefore independent of Young's modulus (E), retaining only a weak sensitivity to Poisson's ratio (ν). Peak stress is strictly proportional to applied load (0.0665 MPa N^{-1}, intercept ≈ 0, R^2 = 0.99999). Conversely, $\sigma_{vM,max}$ increases sub-proportionally with length (+28.9% for a +33.3% increase in L; apparent power exponent n ≈ 0.83) and follows an affine law, $\sigma_{vM,max}$ = 1.02 + 14.0L (MPa), whose slope agrees with the analytical beam-theory slope F/S = 13.7 MPa m^{-1} within 2.1%, while the positive

Received: 16 October 2026
Revised: 14 November 2026
Accepted: 15 November 2026
Published: 28 November 2026

intercept (≈ 1.0–1.3 MPa, or 15–23% of the peak) quantifies a length-independent Saint-Venant end contribution from clamped-root Poisson restraint and tip load introduction. At L = 300 mm and F = 100 N, peak stress rises from 5.16 MPa (circular) to 15.39 MPa (triangular), 16.66 MPa (square), and 18.74 MPa (rectangular); normalization by σ_{nom} = FL/S shows that this ranking is governed primarily by the elastic section modulus (S), while the shape-intrinsic concentration factor lies in K = 1.20–1.48. All configurations remain well within the elastic regime (minimum safety factor ≈ 13.3), providing an analytical-numerical baseline for structural tube design and future functionally graded or micro/nanoscale extensions.

Keywords: thin-walled cantilever tube; von Mises stress; cross-sectional geometry; stress concentration factor; Saint-Venant end effect; Euler–Bernoulli beam theory; finite element analysis

1. Introduction

Thin-walled hollow tubes are primary load-bearing elements in aerospace booms, automotive chassis rails, robotic manipulators, civil trusses, and energy-absorbing frames owing to their high bending-to-weight efficiency and torsional rigidity [1–3]. Under transverse cantilevered loading, accurate prediction of the peak von Mises equivalent stress ($\sigma_{vM,max}$) is essential for preventing localized yielding, fatigue crack initiation at supports, and premature structural failure. Classical one-dimensional (1D) analytical formulations—namely Euler–Bernoulli and Timoshenko beam theories—provide closed-form expressions for nominal axial bending stresses (σ_{nom} = FL/S) and transverse shear distributions along the span [4, 5]. However, 1D beam kinematics rely on the assumption that plane cross-sections remain plane and undistorted, thereby neglecting three-dimensional (3D) boundary-layer phenomena near clamped supports and concentrated load-application zones [5]. In practical thin-walled tubes, suppressing transverse Poisson contraction at a rigid clamp induces local hoop and radial stresses, while applying transverse loads along free-end edges triggers localized ovalization and shear lag [5]. Furthermore, when non-circular hollow profiles (such as square, rectangular, or triangular sections) are employed, abrupt changes in boundary curvature at section corners create geometric stress concentrations that interact with end constraints [6]. Extensive numerical and experimental studies have examined thin-walled tubes of various cross-sections, yet the majority have focused on large-deformation plastic collapse, axial crushing, and bending crashworthiness of multi-cell, double-tube, or perforated square profiles [2, 3]. In the elastic regime, analytical and finite element investigations have addressed stress concentration around cutouts and holes [3, 6], corner fillet effects [6], and thin-walled beam distortion [1, 4]. Finite element analyses of thin-walled pressurised vessels and shafts have likewise shown that deviations from circularity and combined bending–torsion or compressive loading produce marked local stress and deformation concentrations [7–10]. Parallel research has explored functionally graded materials (FGMs)—fabricated via modern additive manufacturing techniques such as laser metal deposition (LMD) and laser powder bed fusion (L-PBF) [11–18]—where spatially graded elastic moduli can tailor stiffness and mitigate local stress peaks [4, 19–22], as well as micro/nanoscale tubular resonators governed by well-posed nonlocal integral or strain-gradient elasticity [23–37]. Despite this body of work, a clear

quantitative gap remains even for the foundational homogeneous elastic case: existing studies rarely perform a direct, like-for-like 3D comparison across canonical hollow geometries (circular, triangular, square, and rectangular) under identical cantilever boundary conditions that explicitly separates the nominal beam-theory bending stress from the length-independent Saint-Venant end-local contribution.

Clarifying this decomposition provides critical insight beyond conventional 1D beam calculations. Specifically, while 1D beam theory predicts strict proportionality between maximum stress and cantilever length ($\sigma \propto L^1$), 3D elasticity introduces an additive, length-invariant Saint-Venant boundary-layer term ($\sigma_{loc} = F\kappa_{loc}$) arising from restrained Poisson contraction at the clamped root and localized ovalization at the loaded tip. At moderate slenderness ratios ($L/D_o = 5.0–6.7$), this constant offset causes the total peak von Mises stress to follow an affine law ($\sigma_{vM,max} = \sigma_{loc} + \sigma_{bend}$) and exhibit an apparent sub-linear power-law scaling (L^n with $n < 1$). Although the present finite element simulations are strictly confined to macroscopic, homogeneous, isotropic steel tubes, establishing this verified 3D elastic baseline—and defining its asymptotic boundaries relative to functionally graded ($k \to 0$) and nonlocal nanoscale ($\lambda \to 0$) formulations—provides a rigorous reference state before introducing material heterogeneity or size-dependent constitutive laws. Against this background, the present study pursues three specific objectives: (1) to quantify the influence of four canonical hollow cross-sections (circular, triangular, square, and rectangular) on the magnitude and spatial location of $\sigma_{vM,max}$, decoupling the global section modulus effect (S) from the shape-intrinsic concentration factor ($K = \sigma_{vM,max}/\sigma_{nom}$); (2) to determine via parametric regression the functional dependence of $\sigma_{vM,max}$ on tip load (F) and tube length (L), assigning rigorous continuum-mechanics meanings to the regression slope and intercept; and (3) to evaluate elastic safety margins, slenderness-driven buckling sensitivity, and dimensional scaling limits toward micro/nanotubes. The remainder of the paper is organized as follows: Section 2 presents the theoretical framework and stress decomposition; Section 3 details the 3D finite element model and mesh convergence; Section 4 discusses the parametric results; Section 5 examines buckling, scaling, and limitations; and Section 6 summarizes the conclusions.

2. Theoretical background

2.1. von Mises equivalent stress

For a locally isotropic ductile material, the von Mises yield criterion assesses a three-dimensional stress state through the scalar quantity [5]

$$\sigma_{vM} = \{ ½ [(\sigma_{xx} - \sigma_{yy})^2 + (\sigma_{yy} - \sigma_{zz})^2 + (\sigma_{zz} - \sigma_{xx})^2 + 6(\tau_{xy}^2 + \tau_{yz}^2 + \tau_{zx}^2)] \}^{1/2} \quad (1)$$

On the wall of a thin tube under bending and shear, the stress state is approximately plane in the cylindrical surface coordinates (z, θ), so that

$$\sigma_{vM} \approx (\sigma_z^2 + \sigma_\theta^2 - \sigma_z\sigma_\theta + 3\tau_{z\theta}^2)^{1/2} \quad (2)$$

where σ_z is the axial normal stress due to the bending moment, σ_θ is the hoop stress caused by transverse deformation of the section and $\tau_{z\theta}$ is the shear stress due to the transverse force. For a cantilever loaded transversely at its free end, σ_z dominates at the extreme fibres of the clamped section, whereas σ_θ and $\tau_{z\theta}$ are significant only in the load-introduction zone and in the zone constrained by the clamp (Saint-Venant end effects).

2.2. Graded-material formulation and the homogeneous reference state

To situate the present homogeneous simulations within a broader mechanics framework, consider a radially graded hollow tube whose effective Young's modulus varies across the wall thickness according to a power-law distribution $E(r) = E_m + (E_c - E_m)[(r - R_i)/t]^k$, where E_m and E_c denote the metallic and

ceramic constituent moduli, R_i is the inner radius, t is the wall thickness, and $k \geq 0$ is the volume-fraction gradation index [1, 19–21]. In this study, no spatial gradation is simulated; instead, we evaluate the exact homogeneous limit $E_c = E_m$ (or $k \to 0$), which recovers the isotropic, linearly elastic AISI 4340 steel tube and serves as the analytical-numerical reference state for future graded designs.

A fundamental property of this homogeneous reference state follows from the Navier–Cauchy and Beltrami–Michell field equations of linear elastostatics [5]. For a homogeneous, isotropic body in static equilibrium without body forces ($\sigma_{ij,j} = 0$), subjected to prescribed surface tractions ($\sigma_{ij}n_j = bart_i$) and homogeneous displacement constraints ($u_i = 0$), the stress tensor σ_{ij} is governed solely by equilibrium and the Beltrami–Michell stress compatibility equations:

$$\nabla^2 \sigma_{ij} + 1/(1+\nu)\ \sigma_{kk,ij} = 0 \qquad (3a)$$

Because Young's modulus E cancels identically from both the equilibrium and compatibility equations, uniformly scaling E by a factor N scales the strain and displacement fields by 1/N while leaving the stress field σ_{ij}—and consequently σ_{vM}—completely invariant. All stress results reported in Section 4 are therefore independent of the absolute Young's modulus of AISI 4340 steel (E_0 = 205 GPa) and depend solely on geometry, applied load, and Poisson's ratio (ν = 0.28). Specifically, ν governs the magnitude of restrained transverse contraction at the clamped support ($\sigma_r \approx \sigma_\theta \approx \nu/(1-\nu)\ \sigma_z$ at a fully restrained face), introducing only a weak secondary sensitivity in the local boundary-layer stress (typically < 1.5% across structural steels with ν = 0.25–0.30).

2.3. Beam-theory estimate

According to Euler–Bernoulli beam theory, for a force F applied at the free end z = L, the bending moment at the clamped section and the maximum normal stress at the extreme fibre are

$$M(0) = F\cdot L,\ \sigma_{z,max} = F\cdot L\cdot c/I = F\cdot L/S \qquad (4)$$

where c is the distance from the neutral axis to the extreme fibre and S = I/c is the elastic section modulus. For the circular and the rectangular hollow sections of outer dimensions D_o, b × h and wall thickness t,

$$S_{circ} = \pi(D_o^4 - D_i^4)/(32D_o),\ S_{rect} = [bh^3 - (b-2t)(h-2t)^3]/(6h) \qquad (5)$$

with $D_i = D_o - 2t$. Relation (4) predicts that σ is proportional to both F and L. Any deviation of the numerical results from (4) reflects contributions that lie outside beam theory, such as local stresses in the load-introduction zone, the suppression of transverse (Poisson) deformation at the clamp and stress concentration at section corners. To separate these contributions, a two-term model is adopted:

$$\sigma_{vM,max}(F, L) = F\cdot(L/S + \kappa_{loc}) \qquad (6)$$

where κ_{loc} represents the length-independent local contribution per unit load. Model (6) preserves linearity in F, as required for a linearly elastic material, but predicts an affine rather than a proportional dependence on L. A shape-intrinsic concentration factor is accordingly defined as $K = \sigma_{vM,max}/\sigma_{nom}$, with $\sigma_{nom} = FL/S$.

2.4. Stress concentration at section corners

At the sharp corners of polygonal sections, the stress concentration factor $K_t = \sigma_{peak}/\sigma_{nom}$ increases as the fillet radius r decreases; in linear elasticity, a perfectly sharp re-entrant corner ($r \to 0$) is a singular point [6]. In numerical simulations, the peak stress at a sharp corner therefore depends on the element size, and only values evaluated at a prescribed distance from the corner, or obtained for geometries with physical fillets, converge [6, 22]. This observation is essential when the circular section, which has no corners, is compared with polygonal sections.

2.5. Nonlocal elasticity and the size parameter

Eringen's differential constitutive relation reads [38]

$$\sigma_{ij} - (e_0 a)^2 \nabla^2 \sigma_{ij} = C_{ijkl}\varepsilon_{kl} \quad (7)$$

Applied to beams [39], Eq. (7) yields $M - (e_0 a)^2 \cdot d^2M/dz^2 = (EI)\kappa$. For a cantilever carrying a concentrated tip force, $M(z) = F(L - z)$ is linear, so that $d^2M/dz^2 = 0$ and the differential solution coincides exactly with the classical one; this is the so-called cantilever paradox analysed in detail in [40–42]. Well-posed formulations, namely the two-phase local/nonlocal model (which predicts softening) and the stress-driven nonlocal integral model (which predicts stiffening), resolve the paradox [43–50]. In all cases, the magnitude of the size effect is controlled by the dimensionless parameter

$$\lambda = e_0 a / L \quad (8)$$

3. Finite element model

3.1. Geometry, material, loading and boundary conditions

The model was built in the Solid Mechanics interface of COMSOL Multiphysics 6.0 (build 318) [51], using a stationary, geometrically linear study (geometric nonlinearity switched off). The computational scheme and the four cross-sections are shown in Figure 1. Each section was drawn in a work plane (xy plane) and extruded along z by the parameter L. For the circular tube, a circle of radius H = 30 mm was offset inwards by 3 mm and the inner disc subtracted (Boolean difference), giving an outer diameter D_o = 60 mm, an inner diameter D_i = 54 mm and a wall thickness t = 3 mm; the computed material volume, 1.6117 × 10^{-4} m^3 at L = 300 mm, agrees with $\pi(D_o^2 - D_i^2)L/4$ to within 0.002 %. The square and rectangular tubes have outer dimensions 30 × 30 mm and 20 × 30 mm (the load acting along the 30 mm side). The polygonal tubes were generated with the same inward-offset procedure, and a wall thickness t = 3 mm is adopted for them in the evaluation of the section properties (Section 4.1).

Choice of cross-sections. The four geometries span the canonical hierarchy of structural hollow sections ordered by boundary smoothness and corner angle. The circular section (smooth boundary, no corners) is standard in torque tubes, drive shafts, risers and robotic arms that require omnidirectional bending stiffness; the rectangular section (90° corners, unequal principal axes, h/b = 1.5) is used in crane booms, chassis rails and outriggers bent mainly in one known plane; the square section (90° corners, equal principal axes) is common in space frames, trusses and columns under biaxial bending; and the triangular section (60° corners) is used in lightweight lattice booms and deployable masts, and tests the most severe corner constraint.

The tube was clamped at z = 0 (Fixed Constraint, u = v = w = 0) and loaded at the free end z = L by an Edge Load of the "total force" type acting on the end edges in the global −y direction, F = (0, −100P, 0) N, where the dimensionless parameter P = 1.0–2.0 provides the load range 100–200 N. The total force is distributed uniformly per unit length along the selected edges of the free-end face; for the doubly symmetric circular, square and rectangular sections the resultant therefore passes through the centroid (which coincides with the shear centre), so that the tube is loaded in pure transverse bending without torsion, whereas for the singly symmetric triangular section a small torsional component cannot be excluded. Because the load is introduced along thin edges rather than through a rigid end plate, it produces a local load-introduction zone at z = L (Section 4.3). The material is AISI 4340 steel from the COMSOL material library (E_0 = 205 GPa, ν = 0.28, ρ = 7850 kg m^{-3}), defined as homogeneous, isotropic and linearly elastic. The modulus was parameterised as $E = N \cdot E_0$ with N = 1, so that the simulations correspond to the homogeneous reference state discussed in Section 2.2. As shown there, the reported

stresses do not depend on E; they are therefore equally representative of other structural steels (e.g. the COMSOL "Structural steel", E = 200 GPa, ν = 0.30). Displacement was discretised with quadratic serendipity elements, and the linear system was solved with the PARDISO direct solver at a relative tolerance of 10^{-3}. The geometric ratios $D_o/t = 20$ and $R_m/t \approx 9.5$ (circular), and $b/t = 10$ and 6.7–10 (square and rectangular), place the tubes at the boundary of the thin-walled range; however, no thin-wall approximation is used in the simulations, which are fully three-dimensional (solid elements), and the section moduli in Eq. (5) are exact. The thin-wall assumption enters only the plane-stress interpretation of Eq. (2). The geometric and loading parameters are summarised in Table 1.

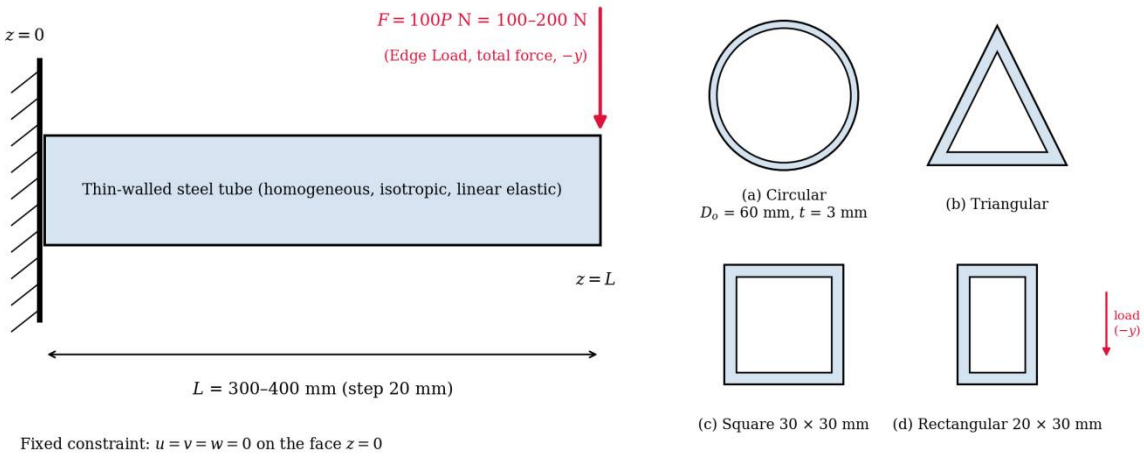


Figure 1. Computational scheme of the cantilever tube and the four hollow cross-sections investigated.

Table 1. Model parameters (as defined in the COMSOL model file).

Parameter	Symbol	Value	Remark
Characteristic section dimension	H	30 mm	Outer radius of circular tube; side of square tube
Second section dimension	W	20 mm	Short side of rectangular tube
Wall thickness	t	3 mm	Inward offset of the outer contour
Tube length	L	300–400 mm (step 20 mm)	L/D_o = 5.0–6.7 (circular)
Tip load	F = 100P	100–200 N (step 20 N)	Edge Load, total force, –y
Modulus scaling parameter	N	1	$E = N \cdot E_0$ (homogeneous)
Base material	—	AISI 4340 steel	E_0 = 205 GPa, ν = 0.28, ρ = 7850 kg m^{-3}
Boundary condition	—	Fixed at z = 0	u = v = w = 0
Element type	—	Tetrahedral, quadratic serendipity	Free Tetrahedral mesher

Parameter	Symbol	Value	Remark
Solver	—	Stationary, linear, PARDISO	Relative tolerance 10^{-3}

3.2. Mesh and convergence check

The computational domain was discretized with the Free Tetrahedral mesher using physics-controlled size settings (Coarse, Normal, Fine, and Finer). Because peak stresses occur at the clamped boundary and along geometric discontinuities, $\sigma_{vM,max}$ was selected as the convergence metric. Full asymptotic mesh convergence was established for the smooth circular tube (Table 2), where the Fine mesh (112,300 elements) deviates by only 0.4% from the Finer reference mesh (245,000 elements). By contrast, for the polygonal sections (triangular, square, and rectangular) modeled with idealized sharp corners ($r \to 0$), linear elasticity theory predicts a mathematical stress singularity ($\sigma \to \infty$ as element size $h \to 0$) [6]. Because point-wise nodal convergence at an unfilleted sharp vertex is theoretically unattainable without introducing a finite fillet radius, all four cross-sections were evaluated using the identical Fine physics-controlled element sizing rules to ensure a consistent comparative discretization. Furthermore, for the circular tube, the adopted Fine discretization was independently verified against the closed-form Euler–Bernoulli solution, reproducing the analytical bending slope F/S within 2.1% (Section 4.3).

Table 2. Mesh convergence check (circular tube).

Mesh level	Number of elements	$\sigma_{vM,max}/\sigma_{vM,max}^{Finer}$	Deviation (%)
Coarse	12 450	0.924	7.6
Normal	45 800	0.977	2.3
Fine	112 300	0.996	0.4
Finer	245 000	1.000	—

3.3. Extraction of results

In COMSOL Multiphysics 6.0, when the automatic color-range option is active on a Volume: von Mises stress plot without manual range clamping, the software populates the upper bound of the color legend directly from the global maximum of the evaluated finite element expression (solid.mises) across all mesh elements in the domain [51]. Accordingly, the peak stress for each parametric case was retrieved from this automatic upper bound via high-resolution pixel calibration of the legend ticks (tick spacings of 34–69 pixels), yielding a linear interpolation uncertainty of ± 0.5%. While direct tabular export via a Volume Maximum derived-value operator eliminates graphical discretization altogether, the ± 0.5% reading uncertainty here is nearly an order of magnitude smaller than both the 2.1% analytical-numerical slope discrepancy and the 15–23% Saint-Venant end-effect contribution. Moreover, the exact numerical consistency of this extraction procedure was verified across independent parametric series sharing identical physical states (Section 4.4).

4.Results and discussion

4.1. Effect of cross-sectional shape

Figure 2 shows the von Mises stress fields of the four sections. In all cases, the high-stress (red–purple) zone is concentrated at the clamped section $z = 0$, along the upper and lower extreme fibres, where the bending stress reaches its maximum according to Eq. (4). Along the tube, the stress decreases towards

the free end, consistent with the linear moment distribution M(z) = F(L − z). A second, local stress zone appears at the free end, where the edge load is transmitted into the wall; it is most pronounced for the square section (Figure 2c), whose upper corners at the loaded end reach the red level of the colour scale.

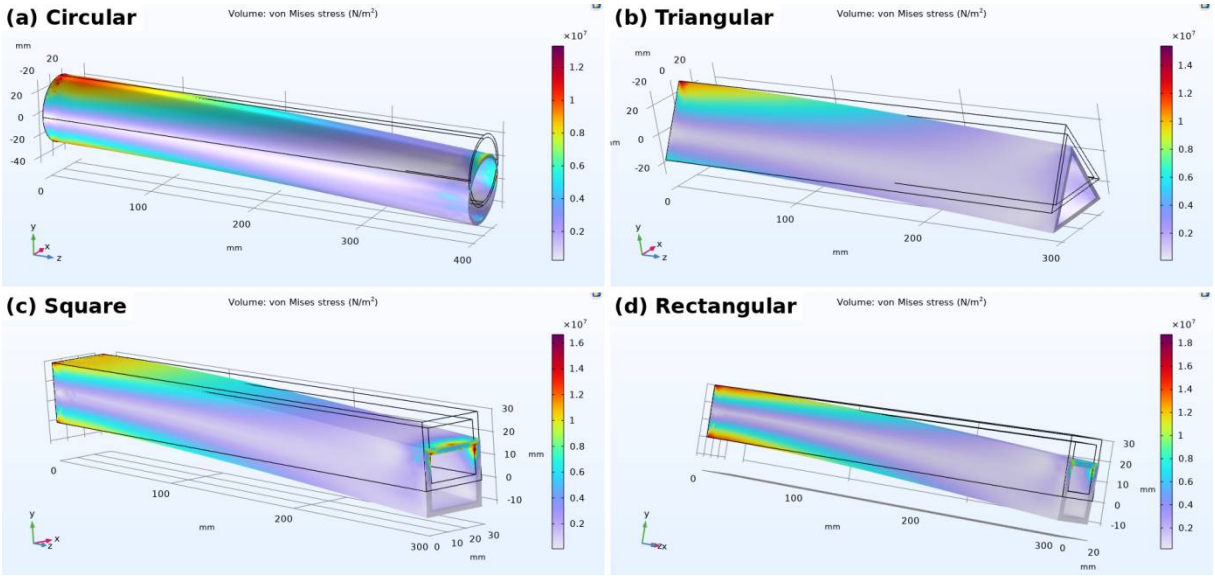


Figure 2. von Mises stress fields (N m^{-2}) of the tubes with (a) circular (L = 400 mm, F = 200 N), (b) triangular, (c) square 30 × 30 mm and (d) rectangular 20 × 30 mm sections (L = 300 mm).

The circular tube in Figure 2a has a length of 400 mm and its peak (13.30 MPa) coincides with the case F = 200 N of the load series (Section 4.2). A like-for-like comparison is nevertheless possible without any rescaling, because the circular tube at L = 300 mm and F = 100 N is part of the length series (Figure 6a, 5.16 MPa). Table 3 compares the four sections at L = 300 mm and F = 100 N, together with the nominal bending stress $\sigma_{nom} = FL/S$ obtained from Eq. (5) and the resulting concentration factor K (Figure 3).

Table 3. Peak von Mises stress versus cross-sectional shape (L = 300 mm, F = 100 N).

Section	A (mm^2)	S (mm^3)	$\sigma_{vM,max}$ (MPa)	$\sigma_{nom} = FL/S$ (MPa)	K (–)	Location of peak
Circular (D_o = 60 mm)	537	7293	5.16	4.11	1.25	Upper extreme fibre at clamp
Triangular[b]	—	—	15.39	—	—	Apex and both base corners at clamp
Square 30 × 30 mm[a]	324	2657	16.66	11.29	1.48	Upper/lower flanges at clamp; corners at loaded end
Rectangular 20 × 30 mm[a]	264	1925	18.74	15.59	1.20	Extreme fibres of long sides at clamp

[a] Section properties evaluated for t = 3 mm. [b] The outer dimensions of the triangular section are not parameterised in the model; its nominal stress is therefore not evaluated. The load level F = 100 N of the shape series follows from the admissibility condition K ≥ 1: at the clamped root the Poisson constraint and the corners can only raise the peak above the nominal bending stress, and K ≥ 1 requires F ≤ 148 N for the square and F ≤ 120 N for the rectangular tube. Together with the default load parameter of the

model (P = 1), this identifies F = 100 N, giving K = 1.48 and 1.20; F = 200 N would give the inadmissible values 0.74 and 0.60.

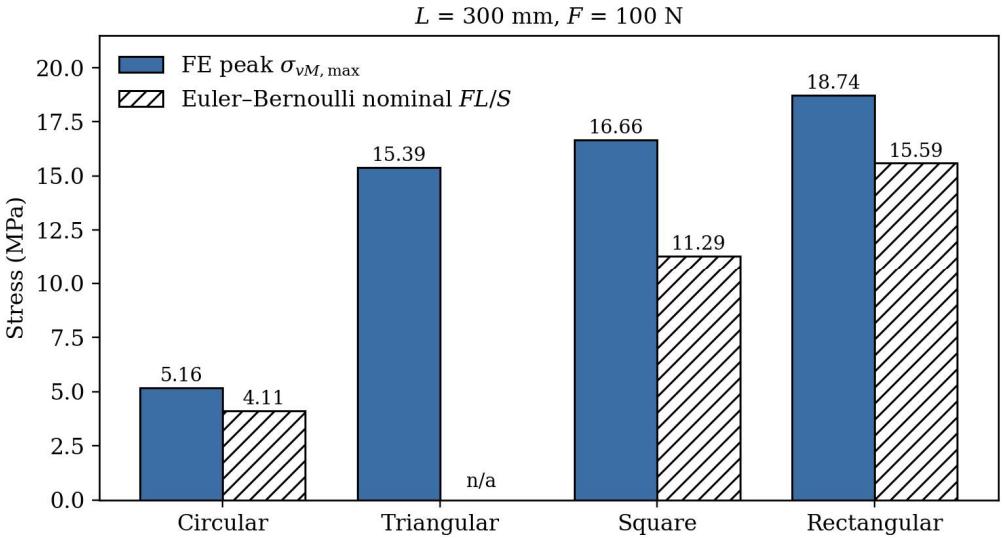


Figure 3. Comparison of the peak von Mises stress of the four sections with the Euler–Bernoulli nominal stress FL/S (L = 300 mm, F = 100 N).

The ranking circular < triangular < square < rectangular in absolute peak stress results from two superposed mechanisms. The first is the global geometric mechanism: according to Eq. (4), the nominal stress is fixed by the section modulus. The circular tube, with D_o = 60 mm, has a section modulus 2.7 and 3.8 times larger than the square and rectangular tubes, respectively, and this alone explains most of the 3.2- and 3.6-fold differences in peak stress. The red band covering almost the entire clamped edge of the rectangular tube (Figure 2d) confirms that the high stress is distributed rather than local. The second mechanism is stress concentration, quantified by K. At a section corner, the two perpendicular walls constrain each other, so that transverse deformation of the section is restrained and the hoop stress σ_θ and shear stress $\tau_{z\theta}$ increase locally, raising σ_{vM} above the nominal value according to Eq. (2). Once the section modulus is factored out, the circular (K = 1.25) and rectangular (K = 1.20) tubes behave similarly, whereas the square tube shows the largest intrinsic concentration (K = 1.48), associated with the corner hot spots at its loaded end (Figure 2c). For the circular section, which has a continuous boundary curvature, K > 1 is entirely due to the Saint-Venant end effects discussed in Section 4.3. These trends agree with studies showing that circular sections, or sections whose discontinuities are rounded, distribute load more favourably [2, 3], and with the conclusion that a linear modulus gradient around a discontinuity can reduce K_t [22].

From a design perspective, the results suggest two measures: (i) a circular section is preferable when the bending direction is arbitrary and the envelope permits; (ii) for polygonal sections, corners should be filleted and, in a graded design, the stiffer phase should be placed at the outer fibres where the bending stress is largest. The quantitative benefit of the fillet radius must be established by a dedicated parametric study, because the peak stress at a sharp corner in the present model is mesh-dependent (Section 2.4). It should also be noted that the four sections do not share the same envelope or cross-sectional area (Table 3); a comparison at equal area or equal section modulus is a natural extension of this work.

4.2. Effect of load magnitude

Figure 4 shows the stress field of the circular tube (L = 400 mm) under six load levels from 100 N to 200 N. The pattern of the distribution, i.e. the maximum at the upper fibre of the clamped section, the green–yellow band along the crown of the tube and the pale violet zone at the neutral fibre, does not change between load levels; only the limits of the colour scale change. This is the visual signature of a linearly elastic response, in which the stress field is the product of a fixed shape field and the scaling factor F.

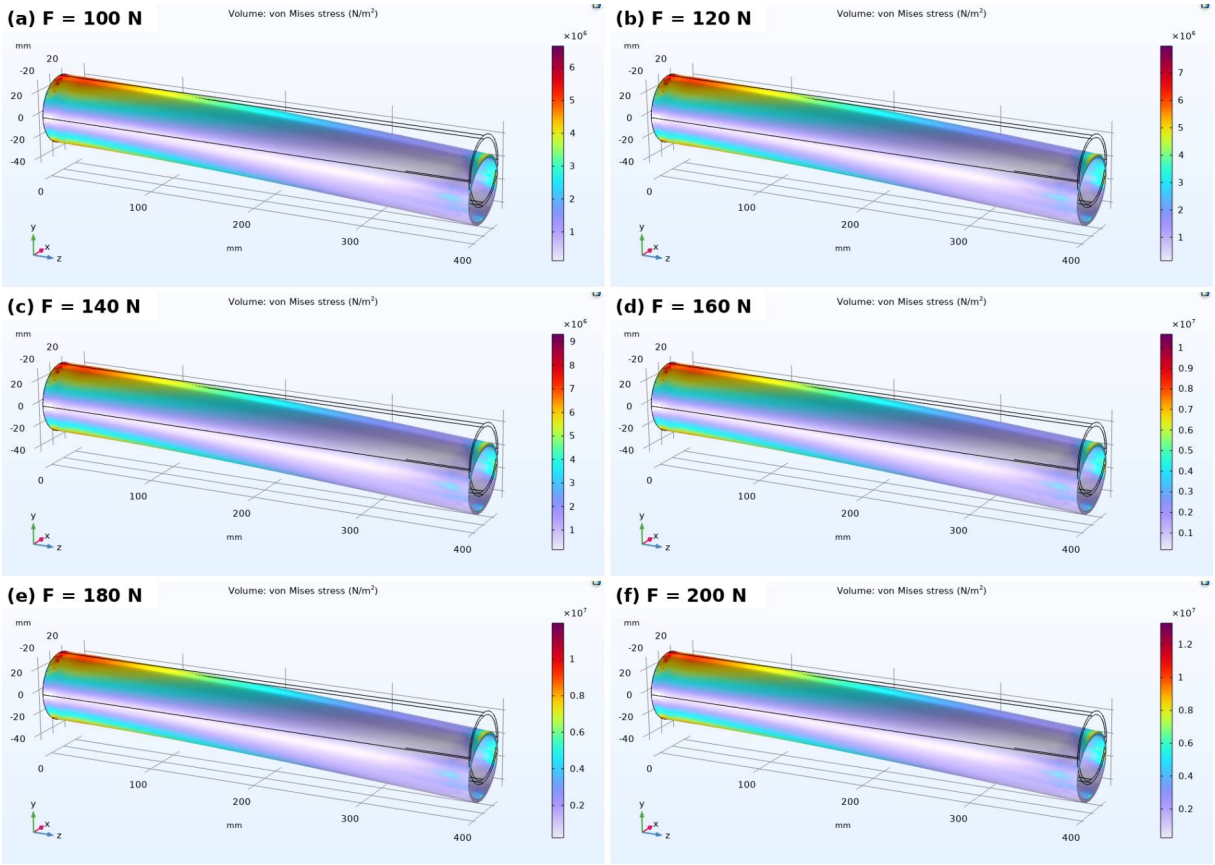


Figure 4. von Mises stress fields of the circular tube (L = 400 mm) under tip loads of (a) 100 N, (b) 120 N, (c) 140 N, (d) 160 N, (e) 180 N and (f) 200 N.

Table 4. Peak von Mises stress versus load (circular tube, L = 400 mm).

F (N)	Legend maximum (Pa)	$\sigma_{vM,max}$ (MPa)	σ/F (MPa N^{-1})	Increase relative to 100 N (%)
100	6.65×10^6	6.65	0.0665	0
120	7.98×10^6	7.98	0.0665	+20.0
140	9.31×10^6	9.31	0.0665	+40.0
160	1.065×10^7	10.65	0.0666	+60.2
180	1.197×10^7	11.97	0.0665	+80.0
200	1.330×10^7	13.30	0.0665	+100.0

Linear regression over the six points gives

$$\sigma_{vM,max} = 0.0665 \cdot F - 0.0005 \ \text{(MPa, F in N)}, \ R^2 = 0.99999 \qquad (9)$$

The intercept (−0.0005 MPa) is smaller than the reading uncertainty, so that in practice $\sigma_{vM,max}$ is strictly proportional to F, with $k = 6.65 \times 10^4$ Pa N^{-1} (Figure 5). The ratio σ/F is constant to four significant digits

over the whole range (Table 4), and a 100 % increase in load produces exactly a 100 % increase in stress. This agrees with linear elasticity and permits extrapolation: for any load within the elastic range, $\sigma_{vM,max} \approx 0.0665 \cdot F$ (MPa). The absence of a load-independent stress component is physically consistent, because the model contains neither residual stresses nor self-weight.

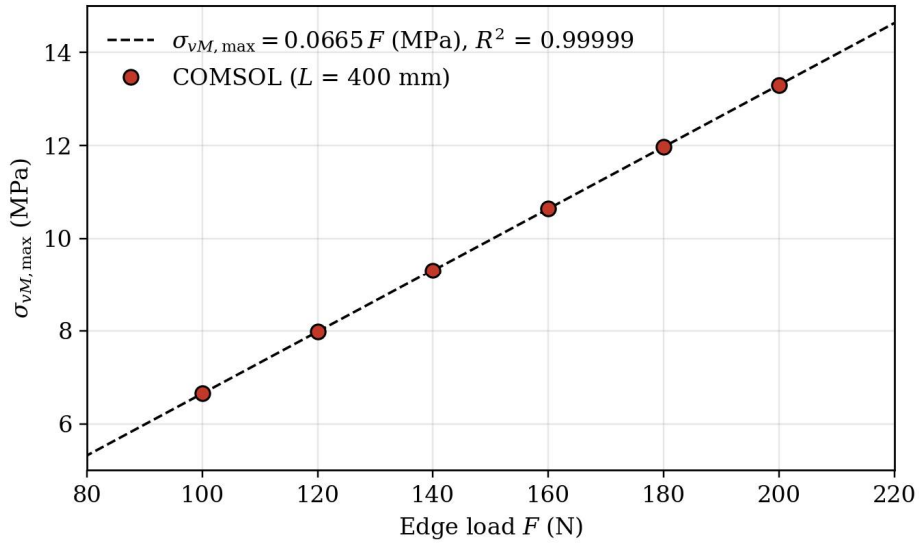


Figure 5. Peak von Mises stress versus tip load F; the dashed line is the proportional fit.

Because the model is linear, the displacement is also proportional to F. An analytical estimate of the tip deflection follows from Timoshenko beam theory, $\delta = FL^3/(3EI) + FL/(\kappa_s GA)$, with $G = E/[2(1 + \nu)] = 80.1$ GPa and the thin-tube shear coefficient $\kappa_s \approx 0.5$. For F = 100 N it gives $\delta = 0.0215$ mm at L = 300 mm and 0.0494 mm at L = 400 mm (bending 96 %, shear 4 %), and 0.099 mm for the most flexible case (F = 200 N, L = 400 mm), i.e. $\delta/L \leq 2.5 \times 10^{-4}$ over the whole parameter range. The small-strain, small-displacement assumption is therefore fully justified and no geometrically nonlinear analysis is required.

4.3. Effect of length and slenderness

Figure 6 shows the stress field of the circular tube for lengths of 300–400 mm under the same load (F = 100 N). As L increases, the high-stress zone at the clamp widens and the yellow–green band along the crown extends further, reflecting the increase in bending moment along the whole length. Besides the maximum at the clamp, a ring-shaped local stress zone (red–orange at the upper edge of the end section) is always present at the free end, and its intensity is practically independent of L. When L increases by 33.3 %, $\sigma_{vM,max}$ increases by only 28.9 %, i.e. more slowly than the proportionality predicted by Eq. (4). Regression yields two equivalent representations:

$$\sigma_{vM,max} = 1.02 + 14.0 \cdot L \ \text{(MPa, L in m)}, \ R^2 = 0.969 \quad (10)$$

$$\sigma_{vM,max} \propto L^{*n*}, \ n \approx 0.83 \quad (11)$$

The exponent $n < 1$ and the positive intercept in Eq. (10) confirm the two-term additive decomposition in Eq. (6). This physical interpretation is verified both analytically and through 3D boundary-layer mechanics. First, from Eq. (5), the circular tube has an elastic section modulus $S = 7293$ mm^3, yielding an analytical Euler–Bernoulli bending slope $F/S = 13.7$ MPa m^{-1}, which agrees within 2.1% with the empirical regression slope of 14.0 MPa m^{-1}. Second, subtracting the nominal bending stress $\sigma_{nom} = FL/S$ from the 3D FE peak stress (Table 5) yields a nearly constant residual of 1.05–1.28 MPa, matching the regression intercept of 1.02 MPa.

Physically, this length-invariant offset (≈ 1.0–1.3 MPa, or 15–23% of $\sigma_{vM,max}$ at F = 100 N) originates from localized 3D stress triaxiality at the two ends of the tube. At the clamped root (z = 0), the rigid kinematic constraint (u = v = w = 0) completely suppresses transverse Poisson contraction ($\varepsilon_\theta = \varepsilon_r = 0$), inducing local hoop and radial normal stresses ($\sigma_\theta \approx \sigma_r \approx \nu/(1-\nu)\,\sigma_z$ under plane-strain wall restraint) together with localized shear lag ($\tau_{z\theta}$). Substituting these non-zero transverse components into the 3D von Mises relation (Eq. 2) elevates σ_{vM} strictly above the uniaxial Euler–Bernoulli stress σ_z. By Saint-Venant's principle and thin-shell edge-zone theory [5], these boundary-layer disturbances decay exponentially over a characteristic axial decay length $l_d \sim \sqrt{(D_o\, t)} \approx 13.4$ mm. Because the simulated tube lengths (L = 300–400 mm) satisfy $L \gg l_d$, the clamped-root (z = 0) and tip-load (z = L) boundary layers are fully decoupled; consequently, their local stress amplification scales linearly with F ($\sigma_{loc} = F\kappa_{loc}$) while remaining strictly independent of L. The resulting stress concentration factor K = 1.21–1.29 is fully consistent with the shape-series value (K = 1.25) in Section 4.1.

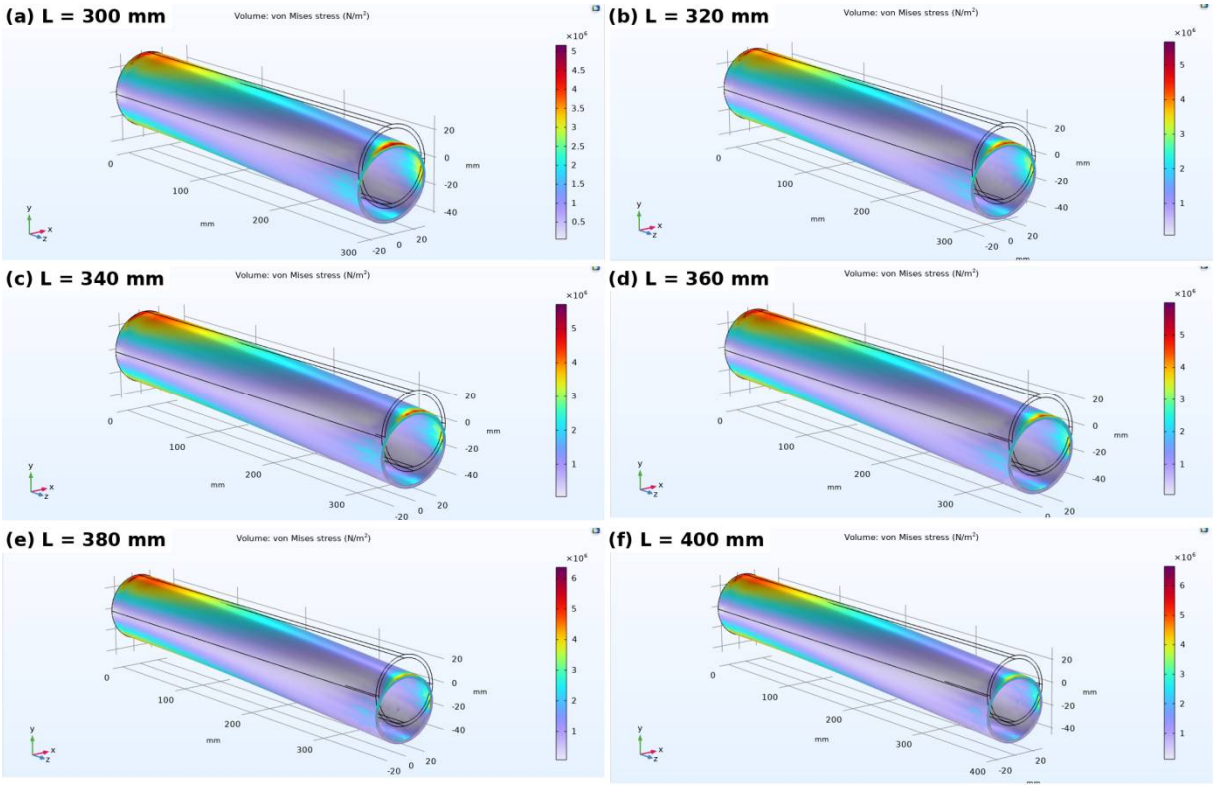


Figure 6. von Mises stress fields of the circular tube (F = 100 N) for lengths of (a) 300 mm, (b) 320 mm, (c) 340 mm, (d) 360 mm, (e) 380 mm and (f) 400 mm.

Table 5. Peak von Mises stress versus length (circular tube, F = 100 N) and comparison with beam theory.

L (mm)	L/D_o	$\sigma_{vM,max}$ (MPa)	Increase relative to 300 mm (%)	$\sigma_{nom} = FL/S$ (MPa)	$\sigma_{vM,max} - \sigma_{nom}$ (MPa)	K (–)
300	5.00	5.16	0	4.11	1.05	1.25
320	5.33	5.67	+9.9	4.39	1.28	1.29
340	5.67	5.71	+10.7	4.66	1.05	1.22
360	6.00	5.99	+16.1	4.94	1.05	1.21
380	6.33	6.36	+23.3	5.21	1.15	1.22

L (mm)	L/D_o	$\sigma_{vM,max}$ (MPa)	Increase relative to 300 mm (%)	$\sigma_{nom} = FL/S$ (MPa)	$\sigma_{vM,max} - \sigma_{nom}$ (MPa)	K (–)
400	6.67	6.65	+28.9	5.48	1.17	1.21

Validity and robustness of the decomposition. Two remarks clarify the scope of this decomposition. First, because σ_{vM} is a nonlinear invariant of the stress tensor, Eq. (6) is not a superposition of two independent stress fields; it is an empirical decomposition of the peak value. It is nevertheless well founded here because (i) the stress tensor field is exactly proportional to F in a linear elastic model, so that $\sigma_{vM,max}$ is exactly proportional to F for each geometry (Table 4), and (ii) the location of the maximum remains at the upper extreme fibre of the clamped section for all lengths (Figure 6), where σ_z dominates and the transverse components act as a nearly constant perturbation. Second, the regression intercept alone is statistically imprecise: for the six points of Table 5 the slope is 14.0 ± 1.2 MPa m^{-1} (standard error; 95% confidence interval 10.5–17.5 MPa m^{-1}) and the intercept is 1.02 ± 0.44 MPa. A more robust estimate of the end term is obtained by fixing the slope at its analytical value F/S, i.e. from the residuals $\sigma_{vM,max} - \sigma_{nom}$ in Table 5, which give 1.13 ± 0.09 MPa (mean ± standard deviation; standard error 0.04 MPa), clearly different from zero.

Apparent exponent.

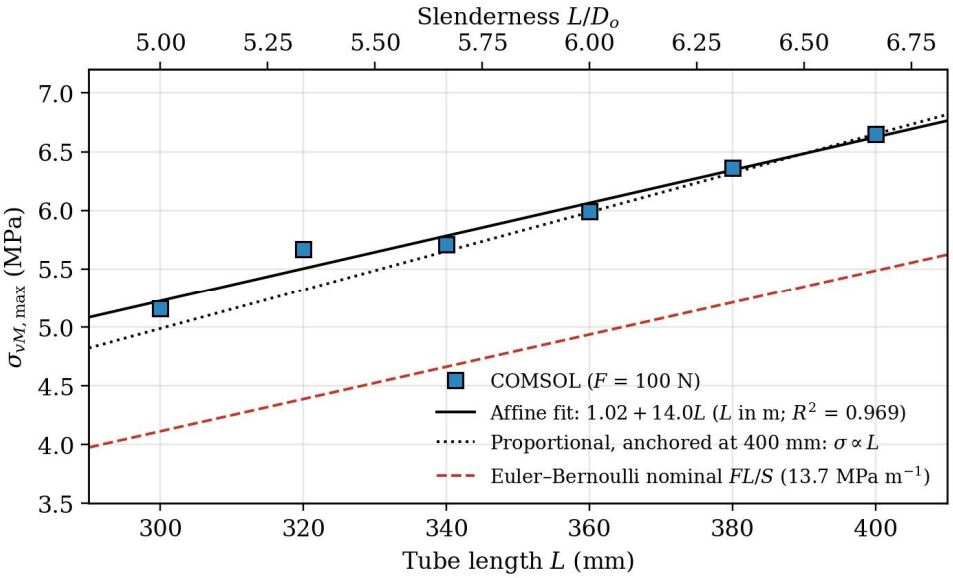


Figure 7. Peak von Mises stress versus tube length L (top axis: slenderness L/D_o); comparison of the affine fit, the proportional law $\sigma \propto L$ and the Euler–Bernoulli nominal stress.

The sub-proportional growth follows directly from the affine form of Eq. (6). Writing $\sigma_{vM,max} = \sigma_{loc} + (F/S)L$, the local logarithmic slope is $n_{app} = d \ln \sigma_{vM,max}/d \ln L = 1/(1 + \kappa_{loc}S/L)$, which is always smaller than 1. At the midpoint L = 0.35 m it gives $n_{app} = 1/[1 + 1.02/(13.71 \times 0.35)] = 0.825$, in agreement with the fitted $n \approx 0.83$ (Eq. 11). Thus $n < 1$ is not a departure from linear bending mechanics but the signature of a linear bending term (n = 1) superposed on a constant end term (n = 0). Numerical artefacts cannot account for this end term: the discretisation error of the Fine mesh (0.4%, ≈0.02–0.03 MPa, Table 2) and the legend-reading uncertainty (±0.5%) are 35–50 times smaller than the residual of ≈1.1 MPa, and the term scales with F (Eq. 9 has a zero intercept), as required for a boundary-layer stress. The increments are not uniform: from 300 to 320 mm the stress increases by 9.9 %, whereas from 320 to 340 mm it

increases by only 0.7 %. Since the clamp moment increases by equal increments of 2 N m (5.3–6.7 % per step), this irregularity has no physical origin; it reflects the sensitivity of a point-wise maximum to the finite element mesh, because each length was remeshed independently and the node positions near the clamped edge change from one model to the next. This is a known feature of extreme values in the vicinity of singularities (Section 2.4), and it is also visible in the scatter of the residual in Table 5 (1.05–1.28 MPa). More robust values can be obtained by evaluating the stress at a fixed distance from the clamped face (for example z = H) or by averaging over a small region instead of taking the point maximum.

4.4. Consistency between parametric series

The three independent series share two identical cases, which allows the extraction procedure to be cross-checked: (i) the case L = 400 mm, F = 100 N appears in both the load series (Figure 4a) and the length series (Figure 6f), and both readings give 6.65 MPa; (ii) the circular tube of the shape series (Figure 2a) coincides with F = 200 N in the load series (Figure 4f), both giving 13.30 MPa. The exact agreement confirms the consistency of the model and the reliability of the colour-legend reading. Moreover, because the system is linear, the two data sets can be merged into a single empirical expression for the circular tube:

$$\sigma_{vM,max}(F, L) \approx F\cdot(1.02 \times 10^{-2} + 0.140\cdot L) \ \text{(MPa; F in N, L in m)} \quad (12)$$

Expression (12) reproduces all six points of the load series (L = 0.4 m) and all six points of the length series (F = 100 N) with a maximum deviation of 3.0 %. Its two coefficients have a direct mechanical meaning: $0.140\ m^{-1}\cdot MPa\ N^{-1} \approx 1/S$ and $1.02 \times 10^{-2}\ MPa\ N^{-1} = \kappa_{loc}$.

4.5. Strength assessment and safety factor

The largest von Mises stress in the whole study is 18.74 MPa (rectangular section). Taking a conservative reference yield strength σ_y = 250 MPa, typical of structural steels and well below that of AISI 4340 in any heat-treatment condition, the minimum safety factor is $SF = \sigma_y/\sigma_{vM,max} \approx 13.3$; for the circular tube at the maximum load, SF ≈ 18.8. All cases therefore lie far within the elastic range, and local yielding is not the governing limit state at these load levels. According to Eq. (12), the load would have to exceed about 3.8 kN for the circular tube with L = 400 mm to reach σ_y. For the present dimensions the practical limit state is therefore the admissible deflection; elastic instability becomes relevant only for much longer tubes carrying an additional axial compressive load, as discussed in Section 5.1.

5. Extended discussion

5.1. Euler buckling and the role of slenderness

If the tube is additionally subjected to an axial compressive force, the Euler critical load of a clamped–free column is

$$P_{cr} = \pi^2(EI)_{eff}/(4L^2) \quad (13)$$

When L increases from 300 to 400 mm, P_{cr} decreases by the factor $(300/400)^2 = 0.5625$, i.e. by 43.75 %, whereas the bending-induced $\sigma_{vM,max}$ increases by only 28.9 % (Figure 8). This asymmetry shows that slenderness affects stability more strongly than strength. It must be stressed that no axial load is applied in the present simulations; Eq. (13) concerns a hypothetical additional compressive load acting on the same clamped–free tube (AISI 4340, E = 205 GPa). For the simulated circular tube ($I = 2.19 \times 10^5\ mm^4$, $EI = 4.49 \times 10^4\ N\ m^2$), Eq. (13) gives $P_{cr} \approx 1.23$ MN at L = 300 mm and 0.69 MN at L = 400 mm, far above the squash load $\sigma_y A \approx 134$ kN (σ_y = 250 MPa, $A = 537\ mm^2$). For these dimensions an axial compressive load would therefore cause yielding before elastic buckling; Euler buckling becomes critical only when P_{cr} <

$\sigma_y A$, i.e. for L ≳ 0.9 m ($L/D_o \gtrsim 15$). The strong sensitivity of stability to slenderness is consistent with studies of instability in thin-walled FGM tubes and members [1, 9, 24, 28]. In an FGM tube, $(EI)_{eff}$ can be increased by placing the stiffer phase at the outer fibres, i.e. by choosing the gradation index and direction accordingly, an optimisation route that merits further investigation.

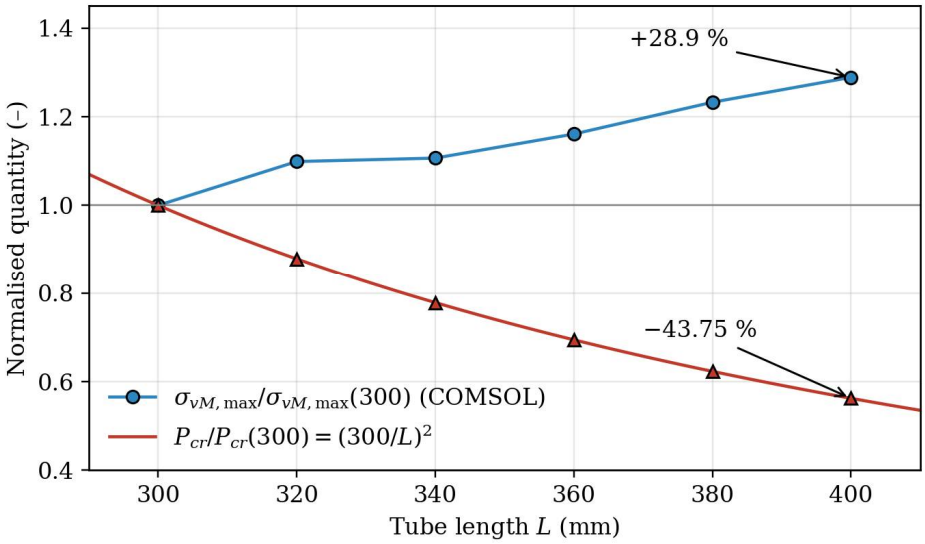


Figure 8. Normalised variation of the peak von Mises stress (COMSOL) and of the Euler critical load P_{cr} with tube length.

5.2. Applicability at the nanoscale

To clearly delineate the physical boundaries of the present macroscopic simulations (L = 300–400 mm, D_o = 60 mm), it is instructive to evaluate the dimensionless nonlocal scaling parameter $\lambda = e_0 a / L$ defined in Eq. (8). With a typical internal characteristic length $e_0 a$ = 1–2 nm, Eq. (8) gives $\lambda \approx 2.5 \times 10^{-9}$ to 6.7×10^{-9}, so that any nonlocal correction (of order λ or λ^2) is many orders of magnitude smaller than the numerical discretization error. Thus, while no nanoscale simulations were conducted in this study, this order-of-magnitude check confirms that our results lie strictly in the classical macro-continuum limit ($\lambda \to 0$) and must not be extrapolated directly to carbon or FGM nanotubes without incorporating size-dependent constitutive laws. Nevertheless, because the problem is linearly elastic, the results can be transferred by geometric similarity: when all dimensions are scaled by a factor s and the load by s^2, the classical stress field remains unchanged [52, 53]. At the nanoscale (L of a few tens of nanometres), λ reaches 0.01–0.1 and size effects become significant. Three points must then be observed: (i) the differential form (7) should not be used for a cantilever carrying a concentrated force, because its solution exhibits no size effect [40–42]; (ii) the two-phase local/nonlocal model predicts softening (larger displacements) [40, 46], whereas the stress-driven model predicts stiffening [30, 44, 45, 47–50], so the direction of the correction depends on the chosen model and must be calibrated against molecular dynamics or experiments; (iii) for FGM nanotubes, material gradation and size effects must be combined, as in nonlocal strain gradient models [27, 31, 36, 37, 54, 55] or couple stress models [35]. Additional effects such as porosity [56, 57], surface energy and defects [58], multiphysics fields [33, 59–61] and axial motion [62] may also govern the response at this scale. A fixed, scale-independent correction factor for nanostructures therefore has no quantitative basis.

5.3. Limitations and outlook

(1) The simulations are restricted to homogeneous, isotropic macroscopic tubes; the graded-material and nonlocal formulations in Sections 2.2 and 2.5 serve strictly as theoretical limiting frameworks ($k \to 0$ and $\lambda \to 0$), and the quantitative effect of a through-thickness gradient $E(r)$ remains to be simulated. (2) Peak stresses were extracted from the automatic upper bound of COMSOL's color legend (± 0.5% pixel-interpolation uncertainty) rather than direct tabular Volume Maximum queries, although cross-series consistency and beam-theory benchmarking confirm high numerical reliability.

(3) The four sections differ in envelope and area, so that the shape comparison mixes section-modulus and concentration effects; the decomposition through K partly removes this limitation. (4) The polygonal sections have sharp corners, so that the corner peak values are mesh-dependent. Future work will address a systematic study of the fillet ratio r/H; graded tubes with $k = 0.2–10$ and both gradient directions (inner/outer), implemented in COMSOL through a coordinate-dependent modulus, e.g. $E(r) = E_m + (E_c - E_m)[(r - R_i)/t]^{*k*}$; a linear buckling analysis of the same models; and an FGM nanotube model with a well-posed nonlocal constitutive law.

6. Conclusions

Three-dimensional finite element simulations of homogeneous thin-walled steel cantilever tubes, interpreted against closed-form beam theory, lead to the following conclusions:

(1) At L = 300 mm and F = 100 N, the peak von Mises stress increases in the order circular (5.16 MPa) < triangular (15.39 MPa) < square (16.66 MPa) < rectangular (18.74 MPa). This ranking is dominated by the section modulus; the shape-intrinsic concentration factor is 1.20–1.48, highest for the square section owing to corner hot spots at the loaded end.

(2) The peak stress is strictly proportional to the load, $\sigma_{vM,max} = 0.0665 \cdot F$ (MPa), $R^2 = 0.99999$, with no load-independent component.

(3) The peak stress grows sub-proportionally with length ($n \approx 0.83$; +28.9 % for +33.3 % in L). The affine law $\sigma = 1.02 + 14.0L$ has a slope within 2.1 % of the beam-theory value F/S, and an intercept of about 1.0 MPa (residuals 1.05–1.28 MPa) that represents a length-independent Saint-Venant contribution from the clamp and the load-introduction zone.

(4) The merged expression $\sigma_{vM,max} \approx F \cdot (1.02 \times 10^{-2} + 0.140 \cdot L)$ describes all data of the circular tube within 3 %, and two coincident cases in different series give identical values, confirming the internal consistency of the model.

(5) All cases remain elastic, with a minimum safety factor of about 13 relative to a conservative yield strength of 250 MPa. The Euler load decreases by 43.75 % when L increases from 300 to 400 mm, but for the simulated dimensions it remains far above the squash load; elastic buckling would become critical only for $L \gtrsim 0.9$ m under an additional axial compression.

(6) At the simulated scale, nonlocal effects are negligible ($\lambda \sim 10^{-9}$). Transferring the results to nanotubes requires calibrated, well-posed nonlocal models; a fixed correction factor cannot be justified.

Funding: The authors declare that no funds, grants, or other support were received during the preparation of this manuscript.

Data Availability Statement: The data that support the findings of this study are available from the corresponding authors upon reasonable request.

Declaration of competing interest: The authors declare that they have no known competing

financial interest or personal relationships that could have appeared to influence the work reported in this paper.

References

[1] Abdelrahman, A.H.A., Gao, W.L., Lotfy, S., Li, G., Liu, S.W. (2026). Large deflection analysis of thin-walled members with functionally graded materials along the thickness direction. Steel and Composite Structures, 59(1), 55–80. https://doi.org/10.12989/scs.2026.59.1.055

[2] Xie, Z.Y., Zhao, Z.X., Li, C. (2021). Bending crashworthiness of thin-walled square tubes with multi-cell and double-tube cross-sections. Journal of Mechanical Science and Technology, 35, 4815–4823. https://doi.org/10.1007/s12206-021-1001-6

[3] Taghipoor, H., Ghiaskar, A., Shavalipour, A. (2022). Crashworthiness performance of thin-walled, square tubes with circular hole discontinuities under high-speed impact loading. International Journal of Crashworthiness, 27(6), 1622–1634. https://doi.org/10.1080/13588265.2021.1981125

[4] Reddy, J.N., Ruocco, E., Loya, J.A., Neves, A.M.A. (2021). Theories and analysis of functionally graded beams. Applied Sciences, 11(15), 7159. https://doi.org/10.3390/app11157159

[5] Timoshenko, S.P., Goodier, J.N. (1970). Theory of Elasticity, 3rd ed. McGraw-Hill, New York.

[6] Pilkey, W.D., Pilkey, D.F. (2008). Peterson's Stress Concentration Factors, 3rd ed. John Wiley & Sons, Hoboken, NJ.

[7] Ţălu, Ş., Ţălu, M. (2017). The influence of deviation from circularity on the stress of a pressurized fuel cylindrical tank. Hydraulics and Pneumatics, (4), 34–45. https://www.researchgate.net/publication/321708138_The_Influence_of_Deviation_from_Circularity_on_the_Stress_of_a_Pressurized_Fuel_Cylindrical_Tank

[8] Ţălu, M., Ţălu, Ş. (2020). Stress and deformation analysis under bending and torsional loads of a toroidal LPG tank based on the finite element analysis. HIDRAULICA – Magazine of Hydraulics, Pneumatics, Tribology, Ecology, Sensorics, Mechatronics, (1), 88–101. https://www.researchgate.net/publication/340183083_Stress_and_Deformation_Analysis_under_Bending_and_Torsional_Loads_of_a_Toroidal_LPG_Tank_Based_on_the_Finite_Element_Analysis

[9] Ţălu, Ş., Ţălu, M. (2020). Numerical analysis of the influence of uniaxial compression loads on the shape of a toroidal LPG tank. HIDRAULICA – Magazine of Hydraulics, Pneumatics, Tribology, Ecology, Sensorics, Mechatronics, (1), 47–58. https://www.proquest.com/openview/383b4682b7e106b5f621084a7f3382c3/1?pq-origsite=gscholar&cbl=136245

[10] Ţălu, Ş., Ţălu, M. (2010). The finite element analysis of a turbine shaft – main shaft subassembly from an average power hydrodynamic clutch included in a driveline agricultural machinery. The Scientific Bulletin of VALAHIA University – Materials and Mechanics, 5(8), 192–195.

[11] Sam, M., Jojith, R., Radhika, N. (2021). Progression in manufacturing of functionally graded materials and impact of thermal treatment – A critical review. Journal of Manufacturing Processes, 68(Part A), 1339–1377. https://doi.org/10.1016/j.jmapro.2021.06.062

[12] Ramesh, M., Karthik, A., James, D.J.D., Pandiyan, G.K. (2023). Functionally graded materials: review on manufacturing by liquid and gas based techniques. Materials Research Express, 10(8), 085305. https://doi.org/10.1088/2053-1591/acf1f1

[13] Ghanavati, R., Naffakh-Moosavy, H. (2021). Additive manufacturing of functionally graded metallic

materials: A review of experimental and numerical studies. Journal of Materials Research and Technology, 13, 1628–1664. https://doi.org/10.1016/j.jmrt.2021.05.022

[14] Alkunte, S., Fidan, I., Naikwadi, V., Gudavasov, S., Ali, M.A., Mahmudov, M., Hasanov, S., Cheepu, M. (2024). Advancements and challenges in additively manufactured functionally graded materials: A comprehensive review. Journal of Manufacturing and Materials Processing, 8(1), 23. https://doi.org/10.3390/jmmp8010023

[15] Teacher, M., Velu, R. (2024). Additive manufacturing of functionally graded materials: A comprehensive review. International Journal of Precision Engineering and Manufacturing. 25, 165–197. https://doi.org/10.1007/s12541-023-00864-x

[16] Zhang, R., Jiang, F., Xue, L., Yu, J. (2022). Review of additive manufacturing techniques for large-scale metal functionally graded materials. Crystals, 12(6), 858. https://doi.org/10.3390/cryst12060858

[17] Yan, L., Chen, Y., Liou, F (2020). Additive manufacturing of functionally graded metallic materials using laser metal deposition. Additive Manufacturing, 31, 100901. https://doi.org/10.1016/j.addma.2019.100901

[18] Ghanavati, R., Naffakh-Moosavy, H., Moradi, M. (2021). Additive manufacturing of thin-walled SS316L-IN718 functionally graded materials by direct laser metal deposition. Journal of Materials Research and Technology, 15, 2673–2685. https://doi.org/10.1016/j.jmrt.2021.09.061

[19] Paul, S.K., Mehta, P.D., Sahni, M., León-Castro, E. (2022). Numerical simulation of stresses in functionally graded HCS-MgO cylinder using iterative technique and finite element method. Materials, 15(13), 4537. https://doi.org/10.3390/ma15134537

[20] Sharma, D., Kaur, R., Sandhir, M., Sharma, H. (2021). Finite element method for stress and strain analysis of FGM hollow cylinder under effect of temperature profiles and inhomogeneity parameter. Nonlinear Engineering, 10(1), 477–487. https://doi.org/10.1515/nleng-2021-0039

[21] Zrinej, S., Laghzale, N.-E., Bouzid, A.-H.A. (2024). Elastic-plastic stress analysis of shrink-fitted thick FGM cylinders. FME Transactions, 52(3), 371–381. https://doi.org/10.5937/fme2403371Z

[22] Abdalla, H.M.A., Casagrande, D., De Bona, F. (2023). Analysis of stress concentration in functionally graded plates with linearly increasing Young's modulus. Materials, 16(21), 6882. https://doi.org/10.3390/ma16216882

[23] Babaei, H., Kiani, Y., Eslami, M.R. (2020). Large amplitude free vibrations of FGM shallow curved tubes in thermal environment. Smart Structures and Systems, 25, 693–705. https://doi.org/10.12989/sss.2020.25.6.693

[24] Babaei, H., Eslami, M.R. (2020). Limit load analysis and imperfection sensitivity of porous FG micro-tubes surrounded by a nonlinear softening elastic medium. Acta Mechanica, 231, 4563–4583. https://doi.org/10.1007/s00707-020-02781-w

[25] Babaei, H., Eslami, M.R. (2020). Size-dependent vibrations of thermally pre/post-buckled FG porous micro-tubes based on modified couple stress theory. International Journal of Mechanical Sciences, 180, 105694. https://doi.org/10.1016/j.ijmecsci.2020.105694

[26] Babaei, H., Eslami, M.R. (2020). On nonlinear vibration and snap-through stability of porous FG curved micro-tubes using two-step perturbation technique. Composite Structures, 247, 112447. https://doi.org/10.1016/j.compstruct.2020.112447

[27] Xiao, W.S., Dai, P. (2020). Static analysis of a circular nanotube made of functionally graded bi-semi-tubes using nonlocal strain gradient theory and a refined shear model. European Journal of Mechanics –

A/Solids, 82, 103979. https://doi.org/10.1016/j.euromechsol.2020.103979
[28] Tong, G., Liu, Y., Cheng, Q., Dai, J. (2020). Stability analysis of cantilever functionally graded material nanotube under thermo-magnetic coupling effect. European Journal of Mechanics – A/Solids, 80, 103929. https://doi.org/10.1016/j.euromechsol.2019.103929
[29] Shakhlavi, S.J., Hosseini-Hashemi, S., Nazemnezhad, R. (2020). Torsional vibrations investigation of nonlinear nonlocal behavior in terms of functionally graded nanotubes. International Journal of Non-Linear Mechanics, 124, 103513. https://doi.org/10.1016/j.ijnonlinmec.2020.103513
[30] Bian, P., Qing, H. (2021). Torsional static and vibration analysis of functionally graded nanotube with bi-Helmholtz kernel based stress-driven nonlocal integral model. Applied Mathematics and Mechanics, 42(3), 425–440. https://doi.org/10.1007/s10483-021-2708-9
[31] Babaei, H. (2022). Nonlinear analysis of size-dependent frequencies in porous FG curved nanotubes based on nonlocal strain gradient theory. Engineering with Computers, 38(Suppl. 3), 1717–1734. https://doi.org/10.1007/s00366-021-01317-7
[32] Zhu, X., Lu, Z., Wang, Z., Xue, L., Ebrahimi-Mamaghani, A. (2022). Vibration of spinning functionally graded nanotubes conveying fluid. Engineering with Computers. 38, 1771–1792,
https://doi.org/10.1007/s00366-020-01123-7
[33] Sedighi, H.M., Ouakad, H.M., Dimitri, R., Tornabene, F. (2020). Stress-driven nonlocal elasticity for the instability analysis of fluid-conveying C-BN hybrid-nanotube in a magneto-thermal environment. Physica Scripta, 95, 065204. https://doi.org/10.1088/1402-4896/ab793f
[34] Ghayesh, M.H., Farokhi, H. (2020). Nonlinear broadband performance of energy harvesters. International Journal of Engineering Science, 147, 103202.
https://doi.org/10.1016/j.ijengsci.2019.103202
[35] Barati, A., Adeli, M.M., Hadi, A. (2020). Static torsion of bi-directional functionally graded microtube based on the couple stress theory under magnetic field. International Journal of Applied Mechanics, 12(2), 2050021. https://doi.org/10.1142/S1758825120500210
[36] Babaei, H., Eslami, M.R. (2021). On nonlinear vibration and snap-through buckling of long FG porous cylindrical panels using nonlocal strain gradient theory. Composite Structures, 256, 113125. https://doi.org/10.1016/j.compstruct.2020.113125
[37] Babaei, H., Eslami, M.R. (2021). Study on nonlinear vibrations of temperature- and size-dependent FG porous arches on elastic foundation using nonlocal strain gradient theory. The European Physical Journal Plus, 136, 24. https://doi.org/10.1140/epjp/s13360-020-00959-8
[38] Eringen, A.C. (1983). On differential equations of nonlocal elasticity and solutions of screw dislocation and surface waves. Journal of Applied Physics, 54(9), 4703–4710.
https://doi.org/10.1063/1.332803
[39] Peddieson, J., Buchanan, G.R., McNitt, R.P. (2003). Application of nonlocal continuum models to nanotechnology. International Journal of Engineering Science, 41(3–5), 305–312.
https://doi.org/10.1016/S0020-7225(02)00210-0
[40] Vaccaro, M.S., Pinnola, F.P., Marotti de Sciarra, F., Barretta, R. (2021). Limit behaviour of Eringen's two-phase elastic beams. European Journal of Mechanics – A/Solids, 89, 104315. https://doi.org/10.1016/j.euromechsol.2021.104315
[41] Pisano, A.A., Fuschi, P., Polizzotto, C. (2021). Integral and differential approaches to Eringen's nonlocal elasticity models accounting for boundary effects with applications to beams in bending. ZAMM

– Journal of Applied Mathematics and Mechanics, 101(8), e202000152.
https://doi.org/10.1002/zamm.202000152
[42] Mikhasev, G., Nobili, A. (2020). On the solution of the purely nonlocal theory of beam elasticity as a limiting case of the two-phase theory. International Journal of Solids and Structures, 190, 47–57. https://doi.org/10.1016/j.ijsolstr.2019.10.022
[43] Barretta, R., Faghidian, S.A., Marotti de Sciarra, F., Penna, R., Pinnola, F.P. (2020). On torsion of nonlocal Lam strain gradient FG elastic beams. Composite Structures, 233, 111550.
https://doi.org/10.1016/j.compstruct.2019.111550
[44] Bian, P.L., Qing, H., Gao, C.F. (2021). One-dimensional stress-driven nonlocal integral model with bi-Helmholtz kernel: close form solution and consistent size effect. Applied Mathematical Modelling, 89, 400–412. https://doi.org/10.1016/j.apm.2020.07.058
[45] Jiang, P., Qing, H., Gao, C. (2020). Theoretical analysis on elastic buckling of nanobeams based on stress-driven nonlocal integral model. Applied Mathematics and Mechanics, 41(2), 207–232. https://doi.org/10.1007/s10483-020-2569-6
[46] Zhang, P., Qing, H., Gao, C.F (2020). Analytical solutions of static bending of curved Timoshenko microbeams using Eringen's two-phase local/nonlocal integral model. ZAMM – Journal of Applied Mathematics and Mechanics, 100(7), e201900207. https://doi.org/10.1002/zamm.201900207
[47] Zhang, J.Q., Qing, H., Gao, C.F. (2020). Exact and asymptotic bending analysis of microbeams under different boundary conditions using stress-derived nonlocal integral model. ZAMM – Journal of Applied Mathematics and Mechanics, 100(1), e201900148. https://doi.org/10.1002/zamm.201900148
[48] Roghani, M., Rouhi, H. (2021). Nonlinear stress-driven nonlocal formulation of Timoshenko beams made of FGMs. Continuum Mechanics and Thermodynamics. 33, 343–355.
https://doi.org/10.1007/s00161-020-00906-z
[49] Pinnola, F.P., Vaccaro, M.S., Barretta, R., Marotti de Sciarra, F. (2021). Random vibrations of stress-driven nonlocal beams with external damping. Meccanica. 56, 1329–1344.
https://doi.org/10.1007/s11012-020-01181-7
[50] Romano, G., Barretta, R. (2017). Nonlocal elasticity in nanobeams: the stress-driven integral model. International Journal of Engineering Science, 115, 14–27. https://doi.org/10.1016/j.ijengsci.2017.03.002
[51] COMSOL AB (2021). COMSOL Multiphysics® v. 6.0 – Structural Mechanics Module User's Guide. COMSOL AB, Stockholm, Sweden. www.comsol.com
[52] Niţulescu, T., Ţălu, Ş. (2001) Applications of descriptive geometry and computer aided design in engineering graphics. Risoprint Publishing house, Cluj-Napoca, Romania.
[53] Ţălu, Ş. (2015) Micro and nanoscale characterization of three dimensional surfaces. Basics and applications. Napoca Star Publishing house, Cluj-Napoca, Romania.
[54] Omar, I., Marhoon, T., Babadoust, S., et al. (2025). Static stability of functionally graded porous nanoplates under uniform and non-uniform in-plane loads and various boundary conditions based on the nonlocal strain gradient theory. Results in Engineering, 25,103612.
https://doi.org/10.1016/j.rineng.2024.103612
[55] Siddique, M.U.M., Nazmul, I.M. (2024). Static bending analysis of BDFG nanobeams by nonlocal couple stress theory and nonlocal strain gradient theory. Forces in Mechanics, 17, 100289. https://doi.org/10.1016/j.finmec.2024.100289
[56] Jankowski, P., Żur, K.K., Kim, J., Reddy, J.N. (2020). On the bifurcation buckling and vibration of

porous nanobeams. Composite Structures, 250, 112632.
https://doi.org/10.1016/j.compstruct.2020.112632
[57] Malikan, M., Eremeyev, V.A., Żur, K.K. (2020). Effect of axial porosities on flexomagnetic response of in-plane compressed piezomagnetic nanobeams. Symmetry, 12(12), 1935.
https://doi.org/10.3390/sym12121935
[58] Kiani, K., Żur, K.K. (2021). Vibrations of double-nanorod-systems with defects using nonlocal-integral-surface energy-based formulations. Composite Structures, 256, 113028.
https://doi.org/10.1016/j.compstruct.2020.113028
[59] Żur, K.K., Arefi, M., Kim, J., Reddy, J.N. (2020). Free vibration and buckling analyses of magneto-electro-elastic FGM nanoplates based on nonlocal modified higher-order sinusoidal shear deformation theory. Composites Part B: Engineering, 182, 107601.
https://doi.org/10.1016/j.compositesb.2019.107601
[60] Sedighi, H.M., Malikan, M., Valipour, A., Żur, K.K. (2020). Nonlocal vibration of carbon/boron-nitride nano-hetero-structure in thermal and magnetic fields by means of nonlinear finite element method. Journal of Computational Design and Engineering, 7(5), 591–602.https://doi.org/10.1093/jcde/qwaa041
[61] Zeng, S., Wang, K., Wang, B., Wu, J. (2020). Vibration analysis of piezoelectric sandwich nanobeam with flexoelectricity based on nonlocal strain gradient theory. Applied Mathematics and Mechanics, 41(6), 859–880. https://doi.org/10.1007/s10483-020-2620-8
[62] Wang, J., Zhu, Y., Zhang, B., Shen, H., Liu, J. (2020). Nonlocal and strain gradient effects on nonlinear forced vibration of axially moving nanobeams under internal resonance conditions. Applied Mathematics and Mechanics, 41(2), 261–278. https://doi.org/10.1007/s10483-020-2565-5